

Check for updates

Polaronic and Electrochemical Signatures in Group IVB (Ti, Zr, Hf) Oxides: Unified SKP-DFT Insights for Tunable Transport in Energy and Electronic Devices

Beatriz Moura Gomes, Júlia Holtz, Maria Luís Pinto, and Maria Helena Braga*

Understanding interfacial energetics and transport mechanisms in transition metal oxides is key to unlocking their potential in microelectronics, memory, and energy harvesting and storage. Here, a unified electrochemical potential scale is established for the group IVB oxides TiO2, ZrO2, and HfO2, combining spatially resolved scanning Kelvin probe microscopy with hybrid and density functional theory (DFT) simulations. These results show good agreement between DFT-predicted absolute chemical potentials and experimental surface potentials across multiple electrode configurations and surface terminations. ZrO₂ exhibits unexpected emergent behavior under open-circuit conditions, forming ordered potential patterns suggestive of internal charge separation and $O^{\delta-}$ transport. TiO₂ shows dynamic sensitivity to contact polarity and termination, while HfO2 reveals elevated, orientation-dependent potentials linked to spontaneous ferroelectricity. Complementary temperature-dependent conductivity and Hall effect measurements expose thermally activated polaronic transport (Fröhlich model), in all three oxides, including sharp transitions and topological conduction thresholds in HfO2. Simulated chargedischarge cycles further demonstrate field-tunable conductivity and mobility. These findings redefine these oxides as active electrochemical materials, not merely inert dielectrics, and provide a predictive framework for rational interface design in reconfigurable electronics and ion-electron hybrid devices.

B. M. Gomes, J. Holtz, M. L. Pinto, M. H. Braga Faculty of Engineering University of Porto R. Dr. Roberto Frias s/n, Porto 4200–465, Portugal E-mail: mbraga@fe.up.pt

B. M. Gomes, M. H. Braga

LAETA

Institute of Science and Innovation in Mechanical and Industrial Engineering

R. Dr. Roberto Frias 400, Porto 4200–465, Portugal

B. M. Gomes, J. Holtz, M. L. Pinto, M. H. Braga

MatER

Materials for Energy Research University of Porto

Porto 4200–465, Portugal



The ORCID identification number(s) for the author(s) of this article can be found under https://doi.org/10.1002/adfm.202509853

© 2025 The Author(s). Advanced Functional Materials published by Wiley-VCH GmbH. This is an open access article under the terms of the Creative Commons Attribution License, which permits use, distribution and reproduction in any medium, provided the original work is properly cited.

DOI: 10.1002/adfm.202509853

1. Introduction

Titanium dioxide (TiO2), zirconium dioxide (ZrO₂), and hafnium dioxide (HfO₂) are Group 4 of the transition metal oxides in which the metal cations—Ti⁴⁺, Zr4+, and Hf4+—share a common tetravalent oxidation state and exhibit significant chemical similarities. These oxides can be employed across various sectors, including energy, environmental, biomedical, and electronic applications,[1-5] A fundamental understanding of their electronic structure, optical response, and surface properties is essential for rationally designing solid-state devices, particularly where these materials serve as active layers, interfaces, or dielectric components.[6-8]

TiO₂ exhibits tunable optical, electrical, and catalytic properties. [9-12] In energy and optoelectronic applications, TiO₂ nanostructures are widely used in ultraviolet UV photodetectors due to their relatively wide bandgap and high photoelectric efficiency. [13] In the biomedical field TiO₂ composites enable flexible electronics and bone tissue engineering by stimulating osteogenic differentiation via surface

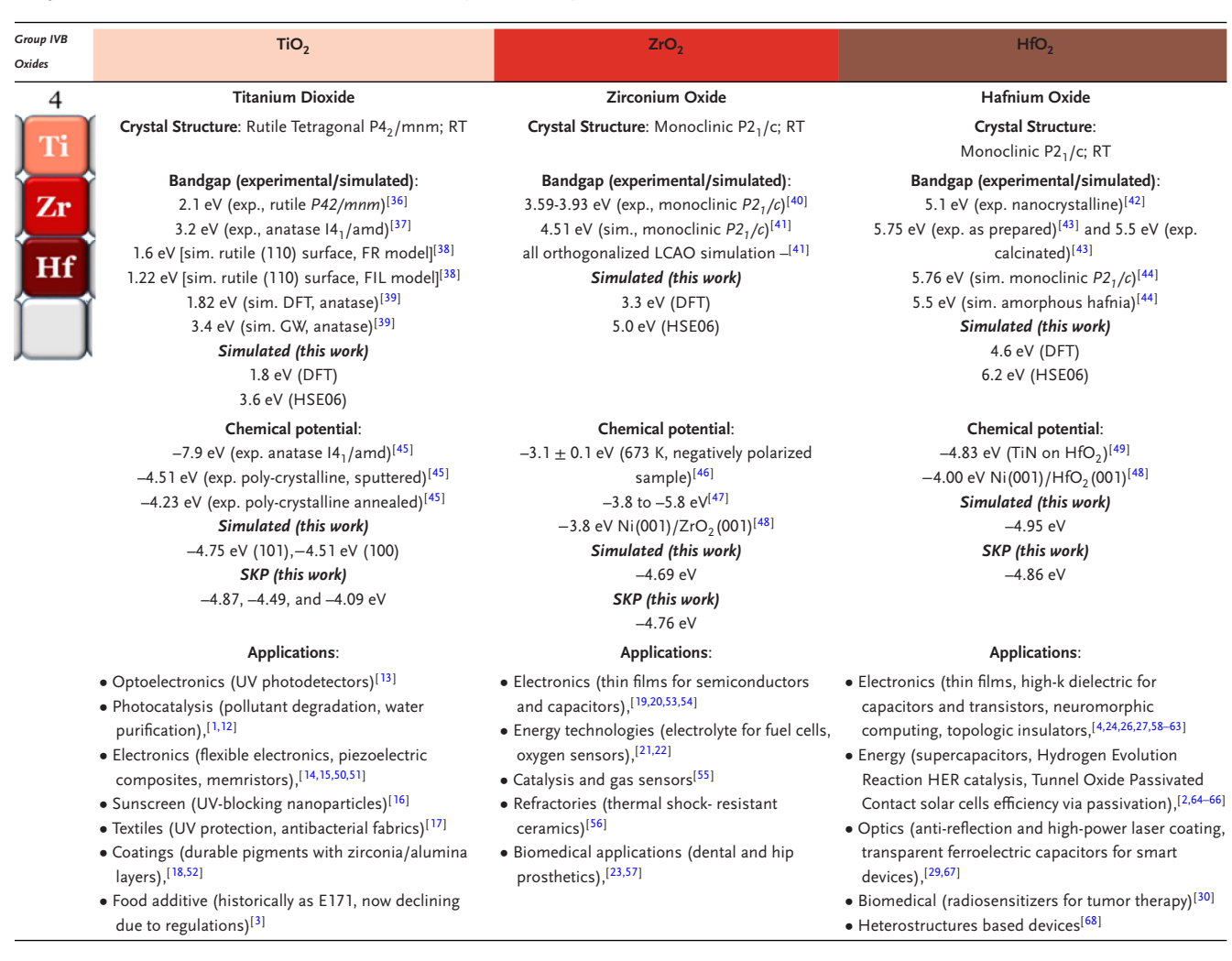
potentials.^[14,15] In consumer and industrial products, TiO₂ UV blocking makes this oxide a common additive in sunscreens.^[16] Its UV protection properties are valuable in the textile industry for self-cleaning fabrics^[17] and protective coatings.^[18]

 $\rm ZrO_2$ is a stable ceramic material with a dielectric constant of approximately $\varepsilon_{\rm r}\approx 16$ and low leakage current, making it a strong candidate for metal-oxide semiconductor devices. [19,20] Its structural and chemical stability supports applications in energy and environmental technologies. Nanostructured $\rm ZrO_2$ is often used to increase surface area for catalysis, sensing, and battery electrodes. [21,22] In biomedical applications, its biocompatibility and mechanical strength (compressive resistance $\sim\!2000\,\rm MPa$) make it suitable for dental implants and orthopaedic prosthetics.

 HfO_2 features a high dielectric constant ($\varepsilon_r \approx 20$ –30), thermal and chemical stability, and can exhibit ferroelectric behavior.^[24] Its orthorhombic ferroelectric phase is crucial in developing non-volatile memory devices such as ferroelectric field-effect transistors and complementary metal-oxide-semiconductor CMOS.^[25–27] HfO_2 is also used

www.afm-journal.de

Table 1. Electronic properties, chemical potential, and applications of the group IVB of oxides TiO_2 , ZrO_2 and HfO_2 . RT: room temperature. DFT: density functional theory; FR: fully relaxing all atom; FIL: layers are fixed to bulk atomic positions; GW: a class of many-body perturbation theory methods; HSE06: Heyd–Scuseria–Ernzerhof hybrid functional; LCAO: orthogonalized linear combination of atomic orbitals. If the surface potential, $\phi_i = 0$, the workfunction WF = $-\bar{\mu}_i = -\mu_i$, where μ_i is the chemical potential of species i.



in anti-reflection coatings due to its optical and mechanical robustness.^[28,29] In high-power laser systems, HfO₂ coatings on ytterbium-doped yttrium aluminum garnet crystals can endure high fluences, even underwater, sometimes outperforming air-based coatings.^[29] In biomedicine, HfO₂:Cu nanocapsules act as radiosensitizers, achieving 77.9% tumor inhibition via X-ray-triggered cuproptosis without detectable toxicity.^[30]

This study focuses on a comparative analysis of TiO₂, ZrO₂, and HfO₂ (**Table 1**). Their shared tetravalent cations and structurally similar frameworks make them ideal for electrochemical benchmarking.^[31–33] Differences in key properties—such as polarizability, ferroelectricity, and potential energy-level alignment—offer valuable insights into surface-dependent behaviors that influence device performance.^[5,32–35] This study combines experimental data, which includes scanning Kelvin probe (SKP) (micro: µm-SKP and nano nm-SKP), sheet resistance, and Hall effect analyses, with computational simulations.

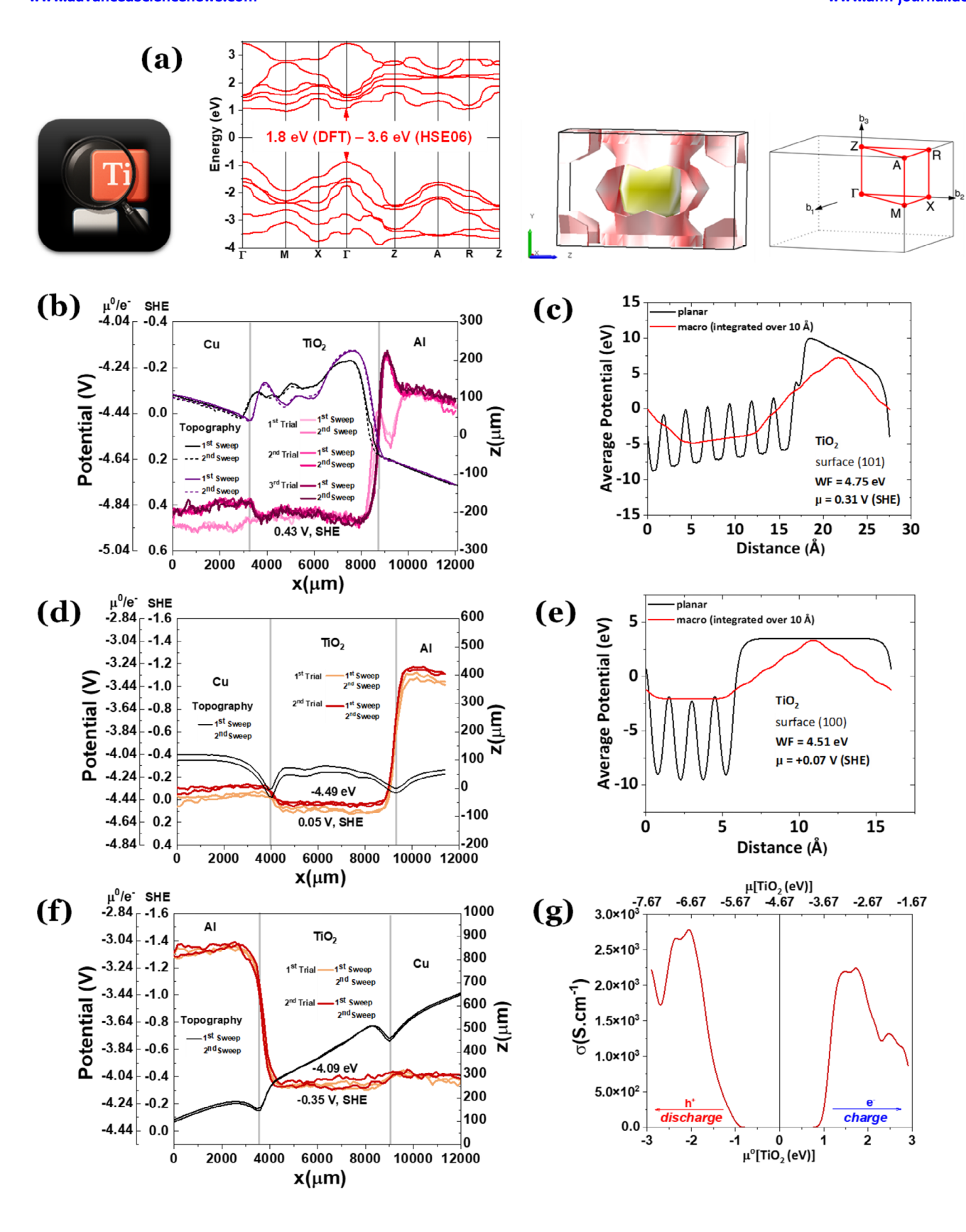
2. Results and Discussion

The DFT-calculated band structure (**Figure 1a**, left) confirms the semiconducting nature of TiO_2 , with a direct bandgap between 1.8 eV (DFT) and 3.6 eV (HSE06), depending on the functional. The HSE06 value is consistent with rutile and anatase polymorphs, albeit 1.8 eV is underestimated as expected from DFT. The constant-energy surface at -2 eV (Figure 1a, right) maps anisotropic occupied states deep in the valence band, reflecting orbital directionality and potential conduction anisotropy under external fields.

We have introduced a novel technique, [69–71] for determining the absolute chemical potential by measuring the surface chemical potential of a cell with a wide gap (4–5 mm) where the dielectric in study is placed as a powder in the gap, in contact with two metals with a chemical potential bias. In the middle of the cell gap, the surface chemical potential of the oxide is approximated to their Fermi level or electrochemical potential, $\bar{\mu}_i = \mu_i + z_i e \phi_i$

16163298, 0, Downloaded from https://advanced.onlinelibrary.wiley.com/doi/10.1002/adfm.20259883, Wiley Online Library on [05/09/2025]. See the Terms and Conditions (https://onlinelibrary.wiley.com/terms-and-conditions) on Wiley Online Library for rules of use; OA articles are governed by the applicable Creative Commons Licenseau Conditions (https://onlinelibrary.wiley.com/terms-and-conditions) on Wiley Online Library for rules of use; OA articles are governed by the applicable Creative Commons Licenseau Conditions (https://onlinelibrary.wiley.com/terms-and-conditions) on Wiley Online Library for rules of use; OA articles are governed by the applicable Creative Commons Licenseau Conditions (https://onlinelibrary.wiley.com/terms-and-conditions) on Wiley Online Library for rules of use; OA articles are governed by the applicable Creative Commons Licenseau Conditions (https://onlinelibrary.wiley.com/terms-and-conditions) on Wiley Online Library for rules of use; OA articles are governed by the applicable Creative Commons Licenseau Conditions (https://onlinelibrary.wiley.com/terms-and-conditions) on Wiley Online Library for rules of use; OA articles are governed by the applicable Creative Commons Licenseau Conditions (https://onlinelibrary.wiley.com/terms-and-conditions) on Wiley Online Library for rules of use; OA articles are governed by the applicable Creative Commons (https://onlinelibrary.wiley.com/terms-and-conditions) on Wiley Online Library for rules of use; OA articles are governed by the applicable Creative Commons (https://onlinelibrary.wiley.com/terms-and-conditions) on Wiley Online Library for rules of use; OA articles are governed by the applicable Creative Commons (https://onlinelibrary.wiley.com/terms-and-conditions) on Wiley Online Library for rules of use; OA articles are governed by the applicable Creative Commons (https://onlinelibrary.wiley.com/terms-and-conditions) on the applicable Creative Commons (https://onlinelibrary.wiley.com/terms-and-conditions) on the applicable Creative Commons (https

www.afm-journal.de





www.afm-journal.de

where μ_i is the absolute chemical potential of the dielectric powder, z_i mobile species valence, e the charge of an electron, and ϕ_i the surface potential of the species i, herein an oxide. If $\phi_i = 0$, the workfunction WF $= -\bar{\mu}_i = -\mu_i$. The theoretical work functions (WF) were converted to electrochemical potentials or absolute chemical potentials (if surface potentials are negligible), by aligning the vacuum level with the standard hydrogen electrode (SHE), using the convention -4.44 eV = 0 V versus SHE.

Micro-SKP measurements of Cu/TiO $_2$ /Al junctions reveal substantial variability in surface potential depending on electrode connection and the sampled surface termination. In Figure 1b, with Cu connected to the μ m-SKP, a surface potential of +0.43 V versus SHE is measured, closely matching the DFT-predicted absolute chemical potential of +0.31 V versus SHE for the (101) surface (Figure 1c). This suggests that the dominant exposed facets are low-energy terminations with stable electrochemical alignment.

The difference in shape between first and subsequent trials, is likely due to the n-type semiconductor character, owing to oxygen vacancies introducing donor levels, allowing transport of electrons to the Cu due to the spontaneous need of aligning the Fermi levels, $\bar{\mu}_i$ and $\bar{\mu}_j$ where $\bar{\mu}_i - \bar{\mu}_j = \mu_i - \mu_j + z_{ij} e(\phi_i - \phi_j)$ and μ_i , μ_j are the absolute chemical potentials, z_{ij} mobile species valence, and ϕ_i , ϕ_j are the surface potentials of species i and j (TiO₂ and Cu or Al). $z_{ij}e$ is the charge exchanged or the charge stored at an electrical double layer capacitor (EDLC) formed at the interface. In this case, if electrons are available at the conduction band of TiO₂ due to impurities, finite temperature, or trapped polarons, they will likely tunnel to the Cu electrode, which has a lower chemical potential. Band bending may also allow electron tunneling from the Al side to the TiO₂ to align the TiO₂/Al Fermi levels.

In a second configuration (Figure 1d), also with Cu connected to the SKP, the potential drops to +0.05 V, which corresponds to the calculated value for the (100) surface (+0.07 V, Figure 1e). This likely results from differences in local crystallographic orientation or stoichiometry of the powder, reinforcing the sensitivity of TiO₂'s surface energetics to subtle morphological factors.

When the polarity is reversed — with Al connected to the SKP (Figure 1f) — a negative surface potential of -0.35 V versus SHE is observed. This inversion underscores the role of electrode work function and interface asymmetry in determining Fermi level alignment and highlights the influence of interfacial dipoles or built-in fields, or even injection of electrons from the Al to TiO_2 . Together, Figure 1b,d,f demonstrate TiO_2 's electrochemical tunability and confirm the μ m-SKP method as a sensitive probe of surface potential influenced by termination, contact direction, and local surface structure.

The simulated conductivity response at 227 °C (500 K) under cyclic charge and discharge (Figure 1g) reveals sharp, reversible

modulations, pointing to field-sensitive conduction mechanisms such as carrier trapping/detrapping or shallow defect activation. These features align with ${\rm TiO_2}$'s well-documented memristive behavior, [50,51,72] and suggest that charge transport is dynamically modulated by internal rearrangement under electrical stress. The temperature-dependent electrical properties of ${\rm TiO_2}$ and ${\rm Al_2O_3}$ (Figures S1 and S2, Supporting Information) exhibit relatively flat trends in sheet resistance and charge carrier concentration, along with lower mobilities, compared to ${\rm ZrO_2}$ and ${\rm HfO_2}$. This contrast highlights key phenomena that are further interpreted using the plasmonic Fröhlich model, which accounts for differences in lattice polarizability.

Finally, the spatially resolved SKP profiles (Figure 1b,d,f) show quasi-flat potential distributions that vary with electrode contact. The observed stabilization or flattening over time (in repeat scans) suggests reversible equilibration of surface charges or defects — likely involving oxygen vacancies or shallow donors — under static electric fields. This internal redistribution underlies the material's capacity to evolve toward electrochemical equilibrium across different configurations, through the electrical contact with electrodes, in an open circuit cell.

In summary, Figure 1 supports a model where ${\rm TiO_2}$ behaves as a versatile electrochemical interface, with measurable potential shifts and transport responses that depend on surface orientation, electrode coupling, and external field conditions. The close agreement between DFT-predicted and SKP-measured chemical potentials strengthens the case for using these complementary tools to design and tune functional oxide materials for memory, catalysis, and energy applications.

Figure 2 presents a detailed analysis of the electronic structure, electrochemical potential, and charge transport behavior of zirconium oxide (ZrO2), integrating DFT predictions with spatially resolved SKP mapping and Hall effect measurements.

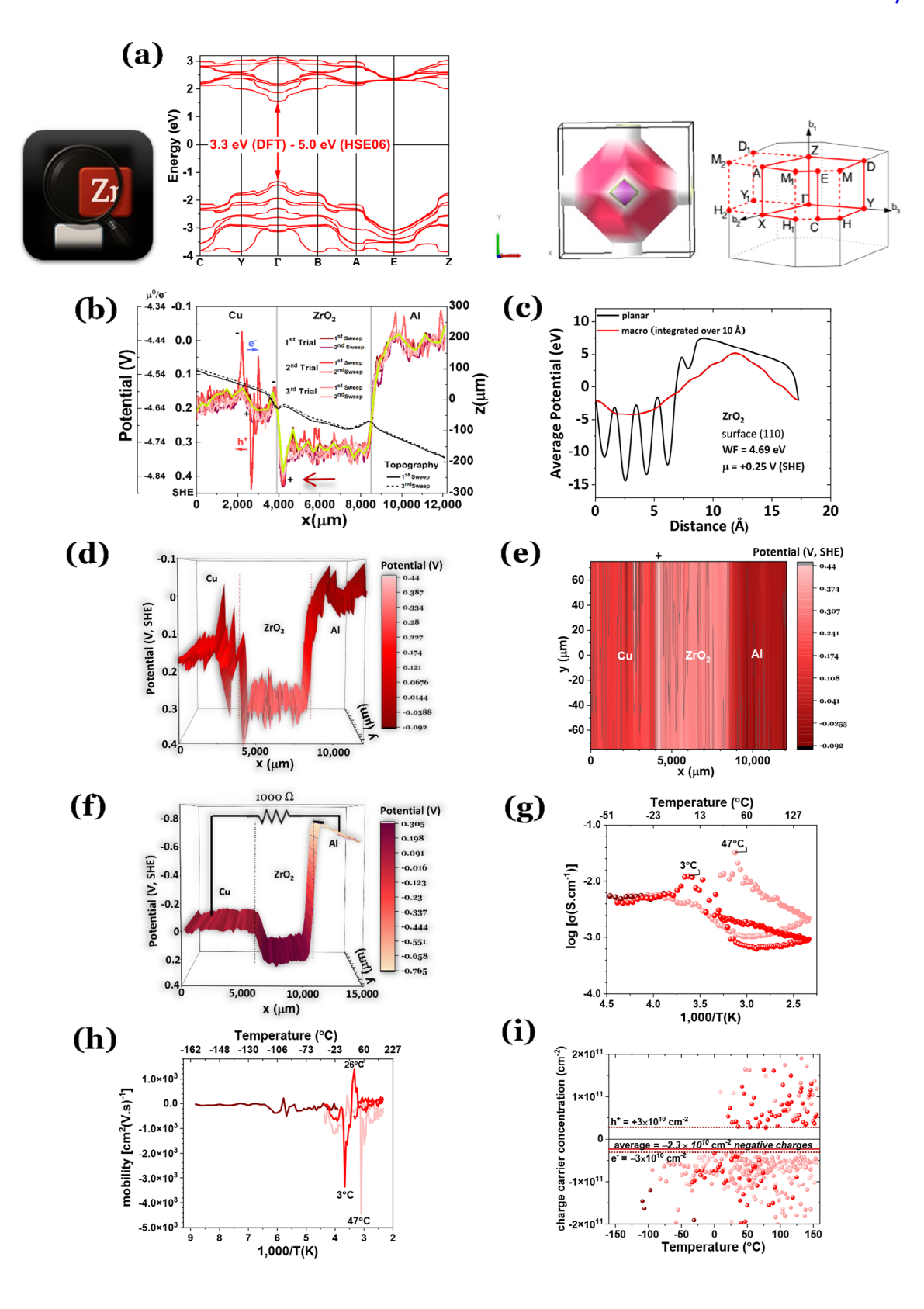
The DFT-calculated band structure (Figure 2a, left) confirms $\rm ZrO_2$'s status as a wide-bandgap insulator, with E $_{\rm g}$ between 3.3 eV (DFT) and 5.0 eV (HSE06), depending on the chosen functional. The constant-energy surface at -2 eV (Figure 2a, right) visualizes the anisotropy of deep valence states, offering insights into the nature of localized states and potential defect interactions.

SKP measurements across a Cu/ZrO $_2$ /Al configuration (\approx 4.5 mm gap, Cu connected to the probe) yield a surface potential of +0.32 V versus SHE, in excellent agreement with the DFT-predicted absolute chemical potential of +0.25 V for the (101) surface (Figure 2c). This consistency validates the application of SKP to powder-based oxides and suggests that surface potential is statistically dominated by low-energy, stable terminations.

A second trial (Figure 2d–e) shows uniform surface potential distributions in both 3D and 2D SKP maps, reinforcing the reproducibility and electrochemical stability of the ZrO₂ interface.

Figure 1. Titanium oxide's electrical and potential properties. a) left: electronic band structure simulated using DFT functional; DFT underestimates the energy of the bandgaps E_g of semiconductors [e.i. 1.8 (DFT) $\leq E_g$ (eV) \leq 3.0 (HSE06)]; right: constant-energy surface that traces all the wavevectors k for which the electron energy E(k) = -2 eV and the corresponding Brillouin zone. It lies below the Fermi surface in energy and represents a deeper occupied state; to the right the Brillouin zone for the primitive tetragonal; E(k) = -2 eV and the corresponding Brillouin zone. It lies below the Fermi surface in energy and represents a deeper occupied state; to the right the Brillouin zone for the primitive tetragonal; E(k) = -2 eV and the curve the primitive tetragonal; E(k) = -2 eV and the energy and represents a deeper occupied state; to the right the Brillouin zone for the primitive tetragonal; E(k) = -2 eV and the energy and represents a deeper occupied state; to the right the Brillouin zone for the primitive tetragonal; E(k) = -2 eV and the energy and represents a deeper occupied state; to the right the Brillouin zone for the primitive tetragonal; E(k) = -2 eV and the corresponding Brillouin zone. It lies below the Fermi surface in energy and represents a deeper occupied state; to the right the electrone in energy and represents a deeper occupied state; to the right the electrone in energy and represents a deeper occupied state; to the right the electrone in energy and represents a deeper occupied state; to the right the electrone in energy and represents a deeper occupied state; to the right the electrone in energy and represents a deeper occupied state; to the right the electrone in energy and represents a deeper occupied state; to the right the electrone in energy and represents a deeper occupied state; to the right the electrone in energy and represents a deeper occupied state; to the right the electrone in energy and represents a deeper occupied state; to the right the electrone in

16163298, 0, Downloaded from https://advanced.onlinelibrary.wiley.com/doi/10.1002/adfm.20259883, Wiley Online Library on [05/09/2025]. See the Terms and Conditions (https://onlinelibrary.wiley.com/terms-and-conditions) on Wiley Online Library for rules of use; OA articles are governed by the applicable Creative Commons Licenseau Conditions (https://onlinelibrary.wiley.com/terms-and-conditions) on Wiley Online Library for rules of use; OA articles are governed by the applicable Creative Commons Licenseau Conditions (https://onlinelibrary.wiley.com/terms-and-conditions) on Wiley Online Library for rules of use; OA articles are governed by the applicable Creative Commons Licenseau Conditions (https://onlinelibrary.wiley.com/terms-and-conditions) on Wiley Online Library for rules of use; OA articles are governed by the applicable Creative Commons Licenseau Conditions (https://onlinelibrary.wiley.com/terms-and-conditions) on Wiley Online Library for rules of use; OA articles are governed by the applicable Creative Commons Licenseau Conditions (https://onlinelibrary.wiley.com/terms-and-conditions) on Wiley Online Library for rules of use; OA articles are governed by the applicable Creative Commons Licenseau Conditions (https://onlinelibrary.wiley.com/terms-and-conditions) on Wiley Online Library for rules of use; OA articles are governed by the applicable Creative Commons (https://onlinelibrary.wiley.com/terms-and-conditions) on Wiley Online Library for rules of use; OA articles are governed by the applicable Creative Commons (https://onlinelibrary.wiley.com/terms-and-conditions) on Wiley Online Library for rules of use; OA articles are governed by the applicable Creative Commons (https://onlinelibrary.wiley.com/terms-and-conditions) on Wiley Online Library for rules of use; OA articles are governed by the applicable Creative Commons (https://onlinelibrary.wiley.com/terms-and-conditions) on the applicable Creative Commons (https://onlinelibrary.wiley.com/terms-and-conditions) on the applicable Creative Commons (https





www.afm-journal.de

Like all the other trials in Figure 2b, it also shows an all-solid-state electrolyte discharge behavior where positive charge accumulates at the interface with the cathode (herein, Cu). $^{[70]}$ In ZrO2, it likely indicates the O $^{\delta-}$ hop to the Al electrode side; leaving Zr $^{4+}$ behind. However, the stripes pattern, evident in both 3D and 2D graphs (Figure 2d–e) and previously observed in the HfO2, $^{[24]}$ highlights the transport in the open circuit Cu/ZrO2/Al cell leading to emergent phenomena throughout the cell to accommodate the initial difference in Fermi levels. This transport may also configure a field dependent Poole-Frenkel's in a metal1/ZrO2/metal2 cell; $^{[73]}$ the same lattice polarizability that leads to Fröhlich polarons also influences trap screening in Poole–Frenkel conduction.

Even if Zirconium dioxide is generally classified as a wide-bandgap n-type semiconductor under most conditions, herein in the cell at OCV analyzed by $\mu\text{m-SKP}$, it behaves as a p-type semiconductor or a discharging mode electrolyte, $^{[70,74]}$ In this case, as shown in Figure 2b, oxygen vacancies introduce donor levels, contributing free electrons to the conduction band, which are likely exchanged with Cu and or Al to align the Fermi levels in the OCV cell, resulting in ZrO $_2$ becoming positively charged. The 2D SKP-experiment includes a positively charged wider strap (light color + band in Figure 2e) and then an orderly thin alternate between negatively and positively charged regions in ZrO $_2$. When the circuit is closed with a 1000 Ω resistor (Figure 2f), the SKP response remains stable, indicating equilibrium-like conditions and a low-leakage dielectric profile.

The log-conductivity versus temperature plot (Figure 2g) shows a distinct transition between ≈3 °C and 47 °C, consistent with activation of carriers from shallow defect states or localized polaron hopping. Supporting this, experimental Hall effect data (Figure 2h-i) confirm a temperature-driven increase in carrier concentration, with a steep rise between 3 °C (negatively charged), 26 °C (positively charged), and 47 °C (negatively charged) — precisely where conductivity increases. This correlation indicates that charge transport in monoclinic ZrO₂ is governed not only by carrier mobility but also by the thermally activated release of trapped carriers or the ionization of oxygen vacancies. The extracted sheet carrier concentration is $\approx -2.3 \times 10^{10}$ cm⁻², corresponding to a charge density of -3.7 nC cm⁻² or 0.61 pg cm⁻² of oxygen released. These vacancies act as donor states, leaving behind localized negative charges. Notably, this value lies well within the measurable range of the Hall effect system, showing a clear window spanning from -3×10^{10} to $+3 \times 10^{10}$ cm⁻². The presence of charge carriers at these magnitudes suggests that thermally activated electrons are excited from donor levels into the conduction band and are subsequently swept away, leaving behind an equal concentration of positively charged oxygen vacancies (denoted Vo in Kröger-Vink notation).

Overall, ZrO₂ exhibits robust and reproducible electrochemical potential behavior and temperature-sensitive conduction characteristics, even in undoped or polycrystalline form. The tight alignment between SKP and DFT establishes a reliable reference potential for ZrO₂, while the temperature-dependent Hall data highlight its latent conductivity modulation, relevant for interface engineering, sensors, or field-effect architectures.

It is highlighted that n-type ZrO₂ semiconductor has applications in gate dielectrics, refractory coatings, and oxygen sensors (especially with n-type conduction due to oxygen vacancies).

Figure 3 explores the structural, electronic, and transport properties of hafnium oxide (HfO₂), combining ab initio simulations with SKP measurements, atomic force microscopy (AFM) imaging, and both experimental and simulated charge transport data.

The DFT-predicted band structure (Figure 3a, left) reveals a large bandgap in the range 4.6–6.2 eV, and the constant-energy surface at –3 eV (Figure 3a, right) maps deep valence states, indicating their potential influence on polarization and defect-driven conduction.

SKP mapping and AFM characterization (Figure 3b,c) of loose HfO₂ powders show an average surface potential of +0.42 V versus SHE, closely matching the DFT-calculated absolute chemical potential of +0.51 V for the (101) surface (Figure 3d). This agreement, observed across multiple trials, [24] confirms the reliability of SKP in characterizing electrochemical behavior even in granular systems with mixed orientations. Figure 3b shows the topography does not match surface chemical potentials, as expected.

It is noteworthy that AFM with nm-SKP is not as reliable as μ m-SKP for determining the absolute chemical potential as the statistics is much less efficient due to a much smaller analyzed zone

Temperature-dependent transport data (Figure 3e) reveal two pronounced conductivity transitions — ≈-85 and 20 °C with additional features on another run near -85, 20, 44 °C. These are echoed in the mobility and charge concentration curves (Figure 3f,g), suggesting that charge transport is governed by temperature-dependent polaron dynamics. The data support a topological polaron conduction model, where polarons form percolative networks (Fröhlich model) that reconfigure or freeze out at discrete temperature thresholds, [24,75-77] The LO phonon modes correspond to lattice vibrations in which ions with opposite effective charges move in opposing directions along the phonon wavevector q, generating long-range macroscopic electric fields in polar crystals. This Coulombic interaction stiffens the restoring force, thereby increasing the phonon frequency relative to the transverse optical (TO) modes. The longitudinal-transverse optical (LO-TO) phonon splitting,[78,79] enhances long-range electron-phonon coupling giving rise to temperature-dependent mobility through Fröhlich polaron and

Figure 2. Zirconium oxide's electrical and potential properties. a) left: electronic band structure simulated using DFT functional; DFT underestimates the energy of the bandgaps E_g of semiconductors [i.e., 3.3 (DFT) ≤ E_g (eV) ≤ 5.0 (HSE06)]; right: constant-energy surface that traces all the wavevectors k for which the electron energy E(k) = -2 eV and corresponding Brillouin zone. It lies below the Fermi surface in energy and represents a deeper occupied state; to the right the Brillouin zone for the primitive monoclinic; $^{[73]}$ b) μm-SKP of a $Cu/ZrO_2/Al$ with a ≈4.5 mm gap with the Cu connected to the SKP showing an average surface potential of +0.32 V, SHE similar to the absolute chemical potential of +0.25 V, SHE obtained by DFT in c); 3D d) and 2D e) μm-SKP of the second trial in (b); f) μm-SKP of a $Cu/ZrO_2/Al$ with a ≈5 mm gap with the Cu connected to the SKP and the circuit closed with an 1000 Ω resistor, SHE; g) experimental log of the electrical conductivity versus temperature showing a transition between 3 and 47 °C; h) experimental Hall effect charge carrier concentration versus temperature; i) experimental charge carrier concentration (ccc) obtained via Hall effect. Note: in (h) and (i) negative mobility and ccc represent negatively charged species' mobility and ccc.

16163028, 0, Downloaded from https://advanced.onlinelibrary.wiley.com/doi/1.01002/adfm.202509853. Wiley Online Library on [05/09/2025]. See the Terms and Conditions (https://onlinelibrary.wiley.com/terms-and-conditions) on Wiley Online Library for rules of use; OA articles are governed by the applicable Creative Commons License

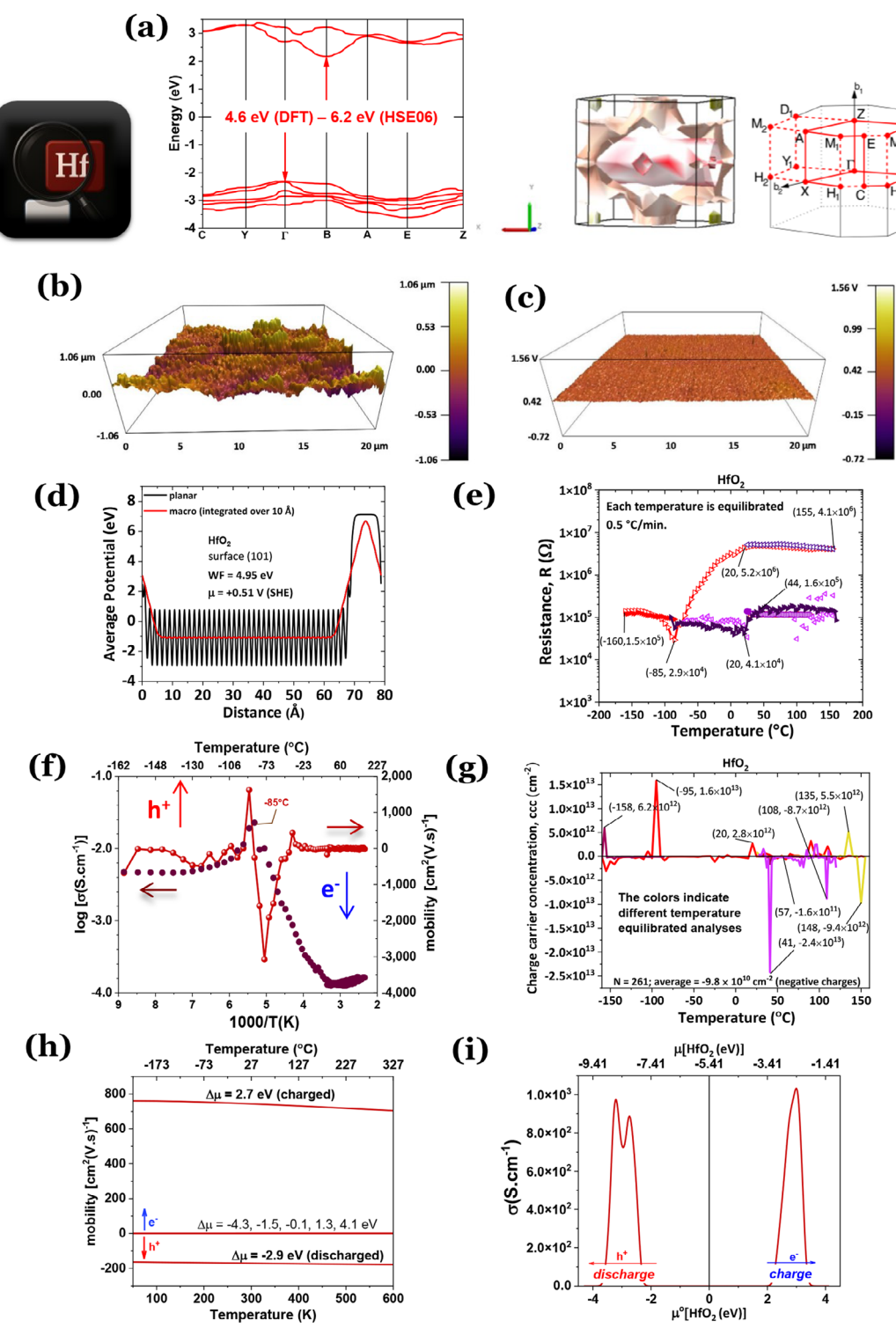


Figure 3. Hafnium oxide's electrical and potential properties. a) left: electronic band structure simulated using DFT functional; DFT underestimates the energy of the bandgaps E_g of insulators [e.i. 4.6 (DFT) $\leq E_g$ (eV) \leq 6.2 (HSE06)]; right: constant-energy surface that traces all the wavevectors k for which the electron energy E(k) = -3 eV and corresponding Brillouin zone. It lies below the Fermi surface in energy and represents a deeper occupied state; to the right the Brillouin zone for the primitive monoclinic; [73] b) and c) AFM/nm-SKP of HfO2 showing an average surface potential of 0.42 V, SHE similar to the absolute chemical potential of 0.51 V, SHE obtained by DFT for a (101) surface in d); e) experimental determination of the sheet resistance showing a transition at 20 °C and another at -85 °C; f) the same transition is observed in the experimental mobility data; g) experimental Hall effect concentration of charge carriers as a function of the temperature h) simulated charge mobility versus temperature charged and discharge HfO₂; i) simulated electrical conductivity versus charge and discharge at 227 °C (500 K). Note: in (g) negative ccc represents negatively charged species.

www.afm-journal.de

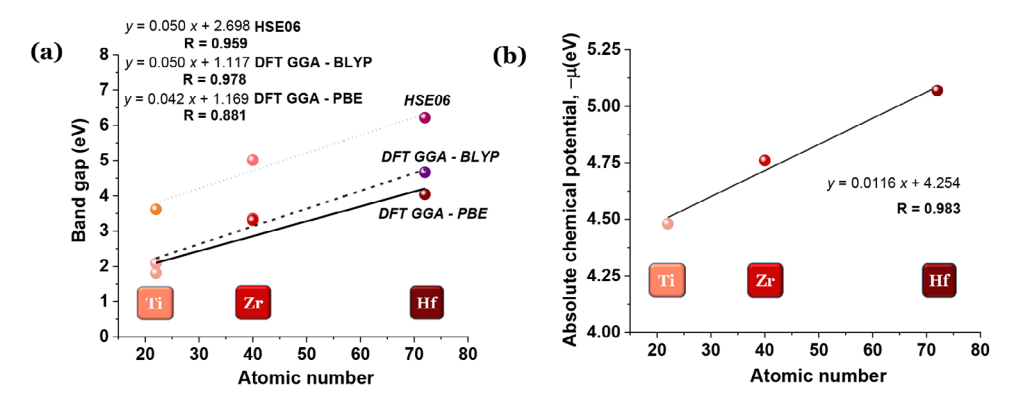


Figure 4. Comparison between simulated bandgap and the average of the experimental absolute chemical potential for TiO_2 , ZrO_2 , and HfO_2 powder measured via scanning Kelvin probe (SKP). a) simulated bandgap versus atomic number; b) average experimental absolute chemical potential versus atomic number. Each data point represents an independent measurement on identically prepared samples (powder), with consistent trends observed across the group IVB oxides. Note: y(x) and its respective correlation R factor result from linear fitting of the data.

confirms the polar nature of $\rm ZrO_2$ and $\rm HfO_2$ and the presence of long-range Coulomb interactions which drive Poole–Frenkel transport in devices. It is noteworthy that the charge carrier concentration (\approx - 10^{11} cm $^{-2}$, n-type semiconductor) in Figure 3g agrees with leakage-free devices with different thicknesses of $\rm HfO_2$ at. $^{[63]}$

Hall carrier concentration data (Figure 3g) reinforce temperature-dependent polaron dynamics picture, showing strong thermally driven variations that align with conductivity inflection points. To support this interpretation, simulations using DFT and Boltzmann transport theory (Figure 3h) replicate the hysteretic behavior of mobility under cyclic charge/discharge, indicating that the observed phenomena are intrinsic to HfO₂'s structure and not artifacts of morphology or measurement.

The simulated mobility in Figure 3h, does not show the experimentally analyzed transitions in Figure 3f. However, away from these critical temperatures, the mobility of the negatively charged species in Figure 1f, reaches 679 cm² (Vs) $^{-1}$ at -160 °C (113 K), while simulated values for $\rm HfO_2$ while charged at 2.7 V, show 760 cm² (Vs) $^{-1}$ at the same temperature, which is a good agreement between experiments and simulations.

Finally, the simulated dynamic conductivity response at 227 °C (500 K) (Figure 3i) demonstrates field-sensitive, reversible modulation — reinforcing the role of metastable internal configurations and field-driven defect dynamics.

Altogether, HfO_2 emerges as a complex, highly tunable oxide, exhibiting both ionic–electronic hybrid conduction and ferroelectric character. The combination of elevated chemical potential, strong DFT–SKP agreement and dynamic polaron transport related to long-range electron-phonon coupling highlights its suitability for memory devices, transistors, topologic insulators based devices and reconfigurable electronic interfaces.

A cross-comparison of TiO₂, ZrO₂, and HfO₂ reveals a coherent trend in both their electronic band structure and surface potential landscapes, unifying their electrochemical behavior on a shared scale (**Figure 4**). The average absolute chemical potential, as captured by SKP and supported by DFT, increases systematically from Ti to Hf, consistent with enhanced polarization and atomic number. ZrO₂ serves as a benchmark of electrochemical stability with minimal variance across configurations, while HfO₂ stands out due to its spontaneous ferroelectricity, leading

to elevated and orientation-sensitive surface potentials. ${\rm TiO_2}$ exhibits dynamic interfacial behavior influenced by surface termination and contact asymmetry. Importantly, all three oxides display temperature-responsive transport features, with transitions attributed to shallow donor activation, polaron hopping, or defect reconfiguration. The combined insights establish these materials not merely as inert dielectrics but as tunable electrochemical interfaces, and the unified scale serves as a guide for rational oxide integration in next-generation electronics and ion-electron hybrid devices.

2.1. Emergent Applications

The oxides investigated in this study exhibited temperature-responsive conductivity phenomena. This behavior can be harnessed for self-powered energy storage devices and thermal sensors, where sharp conductivity variations, with temperature, enable the materials to function as intrinsic thermal thresholds or switches requiring no external bias to detect or respond to thermal stimuli. [80] In energy storage applications, such materials are valuable where steep conductivity gradients near ambient or application-specific temperatures can enhance thermoelectric performance, particularly in hybrid systems. In such cases, polaronic transport may improve carrier mobility while maintaining low lattice thermal conductivity. [81]

Titanium dioxide is a widely studied next-generation, widebandgap (3.2-3.6 eV) n-type semiconductor, known for its strong UV absorption and excellent performance in visible-blind UV photodetectors.^[82] Zheng et al.^[83] reported the scalable fabrication of self-powered TiO2 nanowell-organic hybrid UV photodetectors with tunable performance characteristics. They synthesized three types of inorganic-organic hybrid devices based on ordered TiO₂ nanowalls combined with p-type conductive polyaniline (PANI), resulting in self-powered photodetectors with enhanced sensitivity, wavelength selectivity, fast response, and longterm stability. In a related study, Ghosh et al.[84] developed a broadband self-powered photodetector based on TiO2. The device exhibited strong photoresponse across a wide spectral range (300–1100 nm) under zero-bias operation, demonstrating its potential for highly sensitive detection in both visible and nearinfrared regions.[84]

www.afm-journal.de

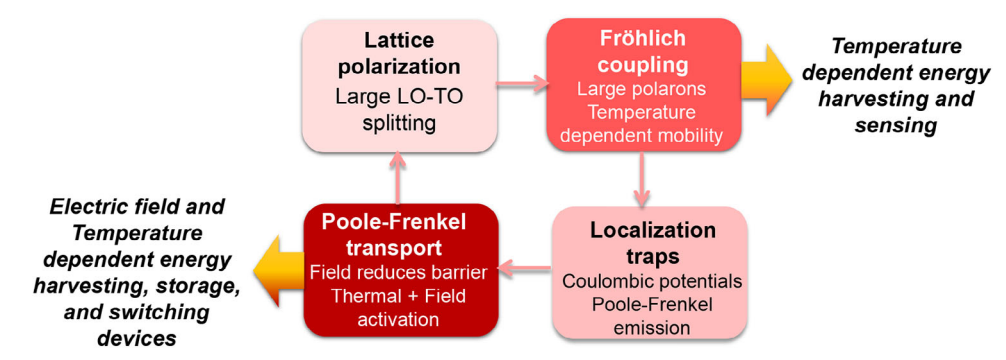


Figure 5. Schematic representation of the interplay between Fröhlich polaron formation and Poole–Frenkel transport mechanisms in the polar oxides ZrO₂ and HfO₂. Lattice polarization, manifested by large longitudinal–transverse optical (LO–TO) phonon splitting, enhances long-range electron–phonon coupling, giving rise to temperature-dependent mobility through Fröhlich polarons, ^[75] which may be harvested in one-electrode devices. Concurrently, the presence of localized Coulombic traps enables Poole–Frenkel conduction, wherein applied electric fields reduce the trap potential barrier, facilitating thermally assisted carrier release. These electric fields are inherently present in capacitors, batteries, or transistor-based architectures—i.e., chemical potential bias devices. The two mechanisms are interconnected, with lattice polarizability governing both polaron mobility and trap-assisted transport dynamics.

Zirconium dioxide has also demonstrated strong potential for being integrated in self-powered smart-sensor platforms. Silva et al. [85] fabricated a transparent Al/Si/SiO_x/ZrO₂/ITO stack incorporating a 5 nm ZrO₂ layer, which couples photovoltaic, pyroelectric, and depolarization fields. This bias-free near-infrared detector achieves a high responsivity of 3.4 A/W, detectivity of 1.2×10^{10} Jones, and sub-4 µs response times at 940 nm. Cho et al.[86] demonstrated that introducing Al₂O₂ into ZrO₂-based metal-insulator-metal capacitors effectively suppresses leakage currents. The resulting ZAZ (ZrO₂/Al₂O₃/ZrO₂) stack showed improved dielectric performance, achieving enhanced capacitance and reduced leakage compared to single-layer configurations. Zheng et al.^[87] engineered a self-powered, broadband photodetector by growing vertically aligned TiO2 nanorod arrays on Fluorine-Doped Tin Oxide glass, coating them with a discontinuous ZrO2 nanoparticle shell, and integrating a metallic singlewalled carbon nanotube (SWCNT) network. The TiO₂|ZrO₂ heterojunction facilitates effective charge separation via type-I band alignment, while the SWCNT mesh ensures efficient charge transport and enhances plasmonic absorption.[87]

Ferroelectric materials are highly suitable for self-powered sensors and high-precision detection systems due to their intrinsic and tunable polarization properties. Among them, HfO2-based resistive switching memory offers several critical advantages, including excellent scalability, fast switching, low power consumption, and full compatibility with standard CMOS technology.[88] These attributes make HfO₂ a strong candidate for high-density and 3D-integrated memory architectures, particularly in neuromorphic computing applications, where artificial synapses are essential for next-generation neural networks. Kumar et al. demonstrated a high-performance, self-powered photosensing and reconfigurable pyro-photoelectric memory device using HfO₂.[89] Their device functions as an infrared pyroelectric sensor with ultrafast response times (as low as 60 µs) and a responsivity of up to 68 μA W⁻¹.^[89] Operating without an external power source, the sensor uses surface heating from pulsed infrared light to induce changes in spontaneous polarization, thereby generating a strong and stable pyro-photocurrent. [89] In a related advancement, Peng et al. developed a 30 nm-thick Ce-doped HfO2 ferroelectric film

exhibiting a high pyroelectric coefficient of $\approx 894.7~\mu C~m^{-2}~K^{-1}$. This enabled the detection of minute temperature variations as small as $0.1~K_{-}^{[90]}$

Their findings highlight the potential of HfO_2 -based ferroelectric materials in self-powered sensors capable of precise temperature and light detection, offering promising emergent properties for integrated, multifunctional sensing platforms, [24] in agreement with the polaronic topologic transport demonstrated herein.

In summary, we propose a mechanism to harvest, store and switch energy from group IVB oxides, especially, ZrO₂ and HfO₂ (**Figure 5**).

3. Conclusion

A unified electrochemical potential framework for ${\rm TiO_2}$, ${\rm ZrO_2}$, and ${\rm HfO_2}$, established through the integration of scanning Kelvin probe microscopy and first-principles DFT simulations is presented. The experimentally measured surface potentials correlate closely with DFT-predicted absolute chemical potentials, validating the approach across distinct surface terminations and electrode configurations.

The absolute chemical potential increases across the series—from Ti to Hf—driven by enhanced polarization and relativistic stabilization. TiO₂ exhibits dynamic surface behavior, sensitive to termination and contact asymmetry. ZrO₂ displays emerging properties to accommodate different interfacial Fermi levels, making it an ideal energy-storage application oxide. HfO₂, in contrast, demonstrates elevated and orientation-dependent potentials consistent with its spontaneous ferroelectric character.

Complementary temperature-dependent conductivity and Hall effect measurements show polaronic and defect-mediated transport mechanisms in all three oxides although more accentuated in ZrO₂ and HfO₂, each exhibiting thermal transitions linked to charge carrier activation and internal reorganization. Simulated charge/discharge responses further show that these materials support field-sensitive, reconfigurable conduction.

Altogether, this work establishes a predictive framework for bandwidth and alignment, interfacial design, and oxide



www.afm-journal.de

pairing in next-generation electronic, memory, and energy devices. Beyond their roles as dielectrics, these oxides emerge as electrochemically active interfaces—capable of tailored functionality, through atomic-scale control of structure, chemistry and temperature.

4. Experimental Section

 TiO_2 Titanium(IV) oxide rutile 99.9% metal basis, 3–6 mm sintered pieces ball milled to \leq 44 μ m, Thermo Scientific, was used in the Cu/TiO₂/Al epoxy cell gap for scanning Kelvin probe analysis, μ m-SKP, sheet resistance, and Hall effect analyses (the latter two analyses are shown in the Supporting Information).

ZrO₂ Zirconium(IV) oxide 99.7% metal basis excluding Hf, with Hf content <75 ppm, 325-mesh powder (\leq 44 μ m), Thermo Scientific, was used in a Cu/ZrO₂/Al cell for μ m-SKP analyses, sheet resistance, and Hall effect analyses.

HfO₂ Hafnium(IV) oxide 99% (metal basis excluding Zr) with Zr < 1.5% from Thermo Scientific with a 325-mesh screen (≤ 44 μ m diameter) was deposited on a glass slide using absolute ethanol and dried prior to analysis by atomic force microscopy and scanning Kelvin probe microscopy (SKPM), nm-SKP.

Methods—Micrometric-Resolution Scanning Kelvin Probe (µm-SKP) and Nanometric-Resolution Scanning Kelvin Probe (nm-SKP): Scanning Kelvin Probe Microscopy (SKPM) was performed using two different devices to achieve both micrometric and nanometric precision. Micrometricresolution SKPM (µm-SKP) was conducted using a Biologic SKP-M470 system equipped with U-SKP-370/1 tips. All measurements were carried out within a dry box. The oxide powders analyzed —TiO2 and ZrO2 were examined in a Cu/oxide/Al epoxy cell configuration. For all measurements, the tip-to-sample distance was maintained at 100 µm. Nanometricresolution SKPM (nm-SKP) was performed using an Oxford Instruments MFP-3D Origin+ atomic force microscope (AFM). This analysis employed a laser-driven ASYELEC-01-R2 tip, with a resonant frequency of ≈75 kHz. The tip was composed of silicon with a reflective Ti/Ir coating and had a spring constant of 2.8 N.m⁻¹. Topography measurements were conducted in tapping mode, where the tip gently oscillates over the sample surface to collect high-resolution surface data. Simultaneously, SKPM data were acquired to map the surface potential distribution. The oxide analyzed via this method was HfO2. These measurements were performed on a glass slide to compare the results with previously reported data for the same material analyzed using the Biologic SKP-M470

Methods—Sheet Resistance and Hall Effect Analyses: Hall effect measurements were conducted using the Linseis HCS 1 system, equipped with two neodymium magnetic circuits on a movable sled. Samples were mounted with edge contacts, and a perpendicular magnetic field of ± 0.7 and 0 T was applied. A constant current (1 nA to 125 mA) passed through the sample, and the resulting Hall voltage, generated orthogonal to both the current and magnetic field, was precisely measured with high sensitivity, from -160 to 160 °C. It was highlighted that each temperature is equilibrated for a heating/cooling rate of $\approx \pm 0.5$ °C min $^{-1}$, therefore emulating ideal thermodynamic cooling/heating.

For sheet resistance analysis, uniformly thick samples were prepared and measured using the Van der Pauw method with four collinear contacts. Current and voltage were applied across different contact pairs in multiple configurations to ensure accuracy. Sheet resistance R_s was determined using the formula $R_s = \frac{V}{l}f$, with correction factor f, and the Van der Pauw relation $e^{-\pi Rs_1/Rs} + e^{-\pi Rs_2/Rs} = 1$. All tests were performed under controlled conditions, with the chamber evacuated to 10^{-2} bar and flushed with nitrogen gas $(4-5 \text{ L min}^{-1})$ to reduce noise, temperature fluctuations, and unwanted reactions.

Methods—Simulation Methods: First-principles calculations were performed using density functional theory (DFT) in conjunction with the generalized gradient approximation (GGA) and an exchange-correlation functional approach such as Perdew–Burke–Ernzerhof (PBE),[91] B3LYP

(Becke, [92] 3-parameter [91] Lee-Yang-Parr [93]) and HSE (Heyd-Scuseria-Ernzerhof). [94] The Perdew-Burke-Ernzerhof (PBE) functional is a generalized gradient approximation (GGA) that incorporates the local electron density and its gradient, while B3LYP is a hybrid functional combining GGA with a fixed fraction of exact Hartree-Fock exchange. In contrast, HSE06 is a range-separated hybrid functional that includes shortrange exact exchange, offering improved accuracy for solid-state calculations with reduced computational cost compared to fully nonlocal hybrid functionals.^[95] These simulations were designed to extract various physical and electronic characteristics similar to what was reported.^[24] Calculations were conducted using the VASP6 (Vienna Ab initio Simulation Package) implementing both standard DFT and the hybrid functional HSE06. Simulation parameters included a plane-wave energy cutoff of 400 or 500 eV, reciprocal space sampling, and a k-point spacing between 0.1 to 0.3 $\hbox{\AA}^{-1}$. The oxides were first optimized for their crystal structures at room temperature (Table 1), by relaxing the atomic positions and allowing the volume and shape to vary. Subsequently, various surfaces with different Miller indices were built with a minimum vacuum gap of 10 Å, to break cell periodicity and emulate the surfaces. Macroscopic average electrostatic potentials were modeled within a 10 Å radius. The work function was determined by evaluating the difference between the surface potential maximum (where electrons are at rest) and the average potential value calculated using the energy of the electron "localized" just before the interface (negative) and the surface potential maximum (positive). Usually, this average value is around zero, in our simulations, and corresponds to the electrochemical potential or Fermi level.

Electronic properties such as band dispersions and density of states, charge carrier concentrations, electrical conductivity, and mobility versus chemical potential at different temperatures were also simulated for the optimized bulk crystal structures. The total and average potential energies of simulated surfaces, with different Miller indices, were also simulated for chemical potential determination.

Supporting Information

Supporting Information is available from the Wiley Online Library or from the author.

Acknowledgements

This work was supported by the Portuguese Foundation for Science and Technology FCT UIDP/50 022/2020 Emerging Technologies—LAETA. This work benefited from Agenda CVB — Cadeia de Valor das Baterias em Portugal, nr. C644864613-00000003, financed by the Recovery and Resilience Plan (PRR) and by European Union and of Agenda NGS — New Generation Storage, nr. C644936001-00000045, investment project nr. 58, financed by the Recovery and Resilience Plan (PRR) and by European Union — NextGeneration EU. B.M.G. and M.H.B. are thankful for the European Union's Horizon Europe research and innovation programme under grant agreement No. 101 069 686 (PULSELION). Views and opinions expressed are those of the author(s) only and do not necessarily reflect those of the European Union or CINEA. Neither the European Union nor the granting authority can be held responsible.

Conflict of Interest

The authors declare no conflict of interest.

Author Contributions

Conceptualization by B.M.G and M.H.B; data collection by All; data analysis by B.M.G. and M.H.B; simulations by M.H.B; writing—original draft by All; state of the art insights, writing—review, editing, and approval of final version by All; funding acquisition and supervision by M.H.B.

6163028, 0, Downloaded from https://advanced.onlinelibrary.wiely.com/doi/10.1002/adfm.202509853. Wiley Online Library on [05/09/2025]. See the Terms and Conditions (https://onlinelibrary.wiley.com/terms-and-conditions) on Wiley Online Library for rules of use; OA articles are governed by the applicable Creative Commons. Licenseance and Conditions (https://onlinelibrary.wiley.com/terms-and-conditions) on Wiley Online Library for rules of use; OA articles are governed by the applicable Creative Commons. Licenseance and Conditions (https://onlinelibrary.wiley.com/terms-and-conditions) on Wiley Online Library.



Data Availability Statement

The data that support the findings of this study are available from the corresponding author upon reasonable request.

Keywords

chemical potential, electronic properties, HfO2, TiO2, ZrO2

Received: April 18, 2025 Revised: June 6, 2025 Published online:

- [1] R. Li, T. Li, Q. Zhou, Catalysts 2020, 10, 804.
- [2] Q. Wang, J. Chen, S. Chen, D. Zhou, Y. Du, Y. Ji, Y. Xiong, J. Ke, W. Zhu, Y. Wang, D. Gao, W.-H. Huang, C.-W. Pao, Y. Sun, Y. Li, M. Shao, Z. Hu, X. Huang, Q. Shao, Adv. Mater. 2025, 37, 2415978.
- [3] G. Bucher, H. El Hadri, O. Asensio, F. Auger, J. Barrero, J.-P. Rosec, Food Control 2024, 155, 110102.
- [4] S. De, presented at Electron Device Technology and Manufacturing Conference, Hong Kong (China), March 2025.
- [5] D. Panda, T.-Y. Tseng, Thin Solid Films 2013, 531, 1.
- [6] Q. Fu, T. Wagner, Surf. Sci. Rep. 2007, 62, 431.
- [7] J. S. Daubert, G. T. Hill, H. N. Gotsch, A. P. Gremaud, J. S. Ovental, P. S. Williams, C. J. Oldham, G. N. Parsons, ACS Appl. Mater. Interfaces 2017, 9, 4192.
- [8] E. Kusano, J. Vacuum Sci. Technol. A 2019, 37, 051508.
- [9] X. Wang, X. Yuan, D. Wang, W. Dong, C. Dong, Y. Zhang, T. Lin, F. Huang, ACS Appl. Energy Mater. 2018, 1, 876.
- [10] Y. Zhao, C. Li, X. Liu, F. Gu, H. Jiang, W. Shao, L. Zhang, Y. He, Mater. Lett. 2007, 61, 79.
- [11] G. K. Dalapati, S. Masudy-Panah, S. T. Chua, M. Sharma, T. I. Wong, H. R. Tan, D. Chi, Sci. Rep. 2016, 6, 20182.
- [12] K. Nakata, A. Fujishima, J. Photochem. Photobiol., C 2012, 13, 169.
- [13] Z. Li, Z. Li, C. Zuo, X. Fang, Adv. Mater. 2022, 34, 2109083.
- [14] J. Zhang, X. Song, S. Cao, Q. Zhu, X. Chen, D. Li, Q. Yuan, Int. J. Biol. Macromol. 2024, 275, 133088.
- [15] J. Liu, Y. Cheng, H. Wang, D. Yang, C. Liu, W. Dou, X. Jiang, H. Deng, R. Yang, *Nano Energy* 2023, 115, 108742.
- [16] S. Sharma, R. K. Sharma, K. Gaur, J. F. Cátala Torres, S. A. Loza-Rosas, A. Torres, M. Saxena, M. Julin, A. D. Tinoco, *Materials* 2019, 12, 2317.
- [17] M. Radetić, J. Photochem. Photobiol., C 2013, 16, 62.
- [18] J. George, C. C. Gopalakrishnan, P. K. Manikuttan, K. Mukesh, S. Sreenish, Powder Technol. 2021, 377, 269.
- [19] B.-O. Cho, J. Wang, L. Sha, J. P. Chang, Appl. Phys. Lett. 2002, 80, 1052.
- [20] D. M. Hausmann, R. G. Gordon, J. Cryst. Growth 2003, 249, 251.
- [21] W.-J. Lee, W. H. Smyrl, Electrochem. Solid-State Lett. 2005, 8, B7.
- [22] J. V. Spirig, R. Ramamoorthy, S. A. Akbar, J. L. Routbort, D. Singh, P. K. Dutta, Sens. Actuators B Chem. 2007, 124, 192.
- [23] P. F. Manicone, P. R. Iommetti, L. Raffaelli, J. Dent. 2007, 35, 819.
- [24] M. H. Braga, A. N. Guerreiro, J. Mater. Chem. C Mater. 2024, 12, 19386
- [25] S. S. Cheema, N. Shanker, S.-L. Hsu, J. Schaadt, N. M. Ellis, M. Cook, R. Rastogi, R. C. N. Pilawa-Podgurski, J. Ciston, M. Mohamed, S. Salahuddin, *Nature* 2024, 629, 803.
- [26] J. Hwang, H. Shin, C. Kim, J. Ahn, S. Jeon, J. Mater. Chem. C Mater. 2025, 13, 214.
- [27] M. Lederer, T. Kämpfe, Appl. Phys. Lett. 2025, 126, 130503.
- [28] C.-C. Wang, L. Meng-Chi, S. Li-Chen, K. Chien-Cheng, *Technologies* (*Basel*) 2025, 13, 11.

- [29] J. Lhermite, L. Lamaignère, Z. Cole, D. Descamps, G. Duchateau, C. Féral, D. Marion, E. Mével, M.-C. Nadeau, S. Petit, A. Rohm, G. Rouzaud, P. Balcou, Opt. Laser Technol. 2025, 183, 112209.
- [30] X. Wang, D. Wang, Y. Liao, X. Guo, Q. Song, W. Liu, C. Gu, S. Du, B. Sun, Z. Gu, *Nano Today* 2025, 61, 102626.
- [31] M. Gutowski, J. E. Jaffe, C.-L. Liu, M. Stoker, R. I. Hegde, R. S. Rai, P. J. Tobin, Appl. Phys. Lett. 2002, 80, 1897.
- [32] W. Zheng, K. H. Bowen, J. Li, I. Dabkowska, M. Gutowski, J. Phys. Chem. A 2005, 109, 11521.
- [33] D. Spassov, A. Skeparovski, A. Paskaleva, N. Novkovski, Thin Solid Films 2016, 614, 7.
- [34] K. Tanabe, Mater. Chem. Phys. 1985, 13, 347.
- [35] G. Teufer, Acta Crystallogr. 1962, 15, 1187.
- [36] J. Tao, T. Luttrell, M. Batzill, Nat. Chem. 2011, 3, 296.
- [37] L. Zheng, P. Yu, K. Hu, F. Teng, H. Chen, X. Fang, ACS Appl. Mater. Interfaces 2016, 8, 33924.
- [38] T. T. Thoa, T. T. Nguyen, H. Van Hung, N. T. M. Hue, Vietnam J. Chem. 2023, 61, 563.
- [39] C. E. Patrick, F. Giustino, J. Phys.: Condens. Matter 2012, 24, 202201.
- [40] L. K. Dash, N. Vast, P. Baranek, M. C. Cheynet, L. Reining, Phys. Rev. B Condens Matter Mater. Phys. 2004, 70, 245116.
- [41] F. Zandiehnadem, R. A. Murray, W. Y. Ching, Phys. B+C 1988, 150, 19.
- [42] H. Padma Kumar, S. Vidya, S. Saravana Kumar, C. Vijayakumar, S. Solomon, J. K. Thomas, J. Asian Ceram. Soc. 2015, 3, 64.
- [43] J. Manikantan, H. B. Ramalingam, B. C. Shekar, B. Murugan, R. R. Kumar, J. S. Santhoshi, Adv. Powder Technol. 2017, 28, 1636.
- [44] P. Ondračka, D. Holec, D. Nečas, L. Zajíčková, J. Phys. D Appl. Phys. 2016, 49, 395301.
- [45] S. Kashiwaya, J. Morasch, V. Streibel, T. Toupance, W. Jaegermann, A. Klein, Surfaces 2018, 1, 73.
- [46] D. Sotiropoulou, S. Ladas, Surf. Sci. 2000, 452, 58.
- [47] Z. Azdad, L. Marot, L. Moser, R. Steiner, E. Meyer, Sci. Rep. 2018, 8, 16251.
- [48] K. Zhong, G. Xu, J.-M. Zhang, R. Liao, Z. Huang, Mater. Chem. Phys. 2016, 174, 41.
- [49] A. Kuriyama, J. Mitard, O. Faynot, L. Brévard, L. Clerc, A. Tozzo, V. Vidal, S. Deleonibus, H. Iwai, S. Cristoloveanu, Solid State Electron. 2007, 51, 1515.
- [50] G. A. Illarionov, S. M. Morozova, V. V. Chrishtop, M. A. Einarsrud, M. I. Morozov, Front. Chem. 2020, 8, 00724.
- [51] J. R. Jameson, Y. Fukuzumi, Z. Wang, P. Griffin, K. Tsunoda, G. I. Meijer, Y. Nishi, Appl. Phys. Lett. 2007, 91, 112101.
- [52] D. Yao, Z. Zhang, X. Liu, Q. Huang, X. Liu, S. Huang, R. Qi, Z. Zhang, S. Liu, L. Zheng, W. Deng, Z. Wang, *Vacuum* 2025, 238, 114287.
- [53] M. H. Boratto, M. Congiu, S. B. O. dos Santos, L. V. A. Scalvi, Ceram. Int. 2018, 44, 10790.
- [54] J. P. B. Silva, R. F. Negrea, M. C. Istrate, S. Dutta, H. Aramberri, J. Íñiguez, F. G. Figueiras, C. Ghica, K. C. Sekhar, A. L. Kholkin, ACS Appl. Mater. Interfaces 2021, 13, 51383.
- [55] A. Husain, S. Ahmad, F. Mohammad, Mater. Today Commun. 2019, 20, 100574.
- [56] R. Kusiorowski, J. Wojsa, B. Psiuk, T. Wala, Ceram. Int. 2016, 42, 11373.
- [57] A. Casucci, C. Mazzitelli, F. Monticelli, M. Toledano, R. Osorio, E. Osorio, F. Papacchini, M. Ferrari, *Dental Mater.* 2010, 26, 751.
- [58] J. Kim, S. Kim, H. Kim, S. Kim, D. Ho, C. Kim, J. Mater. Chem. C Mater. 2025, 13, 3587.
- [59] H. Ryu, S. Kim, Nanomaterials 2020, 10, 1550.
- [60] J. P. B. Silva, K. C. Sekhar, K. Veltruská, V. Matolín, R. F. Negrea, C. Ghica, M. J. S. Oliveira, J. A. Moreira, M. Pereira, M. J. M. Gomes, ACS Appl. Electron. Mater. 2020, 2, 2780.
- [61] Z. Li, T. Wang, J. Meng, H. Zhu, Q. Sun, D. W. Zhang, L. Chen, Mater. Horiz. 2023, 10, 3643.



www.afm-journal.de

- [62] K. Jeong, H. Park, J. Chae, K.-I. Sim, W. J. Yang, J.-H. Kim, S.-B. Hong, J. H. Kim, M.-H. Cho, ACS Appl. Mater. Interfaces 2020, 12, 12215.
- [63] P. Shekhar, S. Shamim, S. Hartinger, R. Schlereth, V. Hock, H. Buhmann, J. Kleinlein, L. W. Molenkamp, ACS Appl. Mater. Interfaces 2022, 14, 33960.
- [64] R. U. Rahman, M. Q. Khokhar, S. Q. Hussain, H. Mehmood, H. Yousuf, J. A. Jony, S. Park, J. Yi, Curr. Appl. Phys. 2024, 63, 96.
- [65] A. Mumtaz, J. Iqbal, M. Mumtaz, H. Nawaz, M. Ameen, J. Alloys Compd. 2025, 1012, 178459.
- [66] A. Mumtaz, J. Iqbal, M. Mumtaz, M. Oneeb, Energy 2025, 324, 136042.
- [67] S. Samanta, G. Anoop, W. Seol, H. Joh, S. M. Park, J. Y. Jo, J. Alloys Compd. 2025, 1010, 178235.
- [68] M. He, T. Yao, X. Yan, B. Qiao, Z. Qian, Y. Jiang, M. Tian, Z. Yang, C. Chen, Micron 2025, 190, 103762.
- [69] A. N. Guerreiro, M. C. Baptista, B. A. Maia, M. H. Braga, ACS Appl. Energy Mater. 2022, 5, 9811.
- [70] A. N. Guerreiro, B. A. Maia, H. Khalifa, M. C. Baptista, M. H. Braga, Batteries 2022. 8, 232.
- [71] B. A. Maia, B. M. Gomes, A. N. Guerreiro, R. M. Santos, M. H. Braga, J. Phys. Mater. 2024, 7, 025001.
- [72] G. A. Illarionov, S. M. Morozova, V. V. Chrishtop, M. A. Einarsrud, M. I. Morozov, Front. Chem. 2020, 8, 00724.
- [73] W. Setyawan, S. Curtarolo, Comput. Mater. Sci. 2010, 49, 299.
- [74] B. M. Gomes, J. F. R. Moutinho, M. H. Braga, J. Mater. Chem. A Mater. 2024, 12, 690.
- [75] W. Zheng, B. Sun, D. Li, S. M. Gali, H. Zhang, S. Fu, L. Di Virgilio, Z. Li, S. Yang, S. Zhou, D. Beljonne, M. Yu, X. Feng, H. I. Wang, M. Bonn, *Nat. Phys.* 2022, 18, 544.
- [76] A. N. Guerreiro, I. B. Costa, A. B. Vale, M. H. Braga, Int. J. Mol. Sci. 2023, 24, 15985.
- [77] P. M. M. C. de Melo, J. C. de Abreu, B. Guster, M. Giantomassi, Z. Zanolli, X. Gonze, M. J. Verstraete, npj Comput. Mater. 2023, 9, 1.

- [78] B. Zhou, H. Shi, X. D. Zhang, Q. Su, Z. Y. Jiang, J. Phys. D Appl. Phys. 2014, 47, 115502.
- [79] A. Kersch, R. Ganser, M. Trien, Front. Nanotechnol. 2022, 4, 1026286.
- [80] Huang L., Chen J., Yu Z., Tang D., Anal. Chem. 2020, 92, 2809.
- [81] X. Mettan, J. Jacimovic, O. S. Barisic, A. Pisoni, I. Batistic, E. Horváth, S. Brown, L. Rossi, P. Szirmai, B. Farkas, H. Berger, L. Forró, *Commun. Phys.* 2019, 2, 123.
- [82] H. Zhang, T. Abdiryim, R. Jamal, J. Li, H. Liu, A. Kadir, D. Zou, Y. Che, N. Serkjan, J. Alloys Compd. 2022, 899, 163279.
- [83] L. Zheng, P. Yu, K. Hu, F. Teng, H. Chen, X. Fang, ACS Appl. Mater. Interfaces 2016, 8, 33924.
- [84] C. Ghosh, A. Dey, I. Biswas, R. K. Gupta, V. S. Yadav, A. Yadav, N. Yadav, H. Zheng, M. Henini, A. Mondal, Nano Mater. Sci. 2024, 6, 345
- [85] N. E. Silva, A. R. Jayakrishnan, A. Kaim, K. Gwozdz, L. Domingues, J. S. Kim, M. C. Istrate, C. Ghica, M. Pereira, L. Marques, M. J. M. Gomes, R. L. Z. Hoye, J. L. MacManus-Driscoll, J. P. B. Silva, Adv. Funct. Mater. 2025, 35, 2416979.
- [86] H. J. Cho, Y. D. Kim, D. S. Park, E. Lee, C. H. Park, J. S. Jang, presented at 2006 European Solid-State Device Research Conference, Montreux, Switzerland, September 2006.
- [87] R. Zheng, et al., J. Sci.: Adv. Mater. Devices 2022, 7, 100492.
- [88] S. Brivio, S. Spiga, D. Ielmini, Neuromorph. Comput. Eng. 2022, 2, 042001.
- [89] M. Kumar, H. Seo, Adv. Mater. 2022, 34, 2106881.
- [90] J. Peng, J. Jiang, S. Yuan, P. Hou, J. Wang, J. Materiomics 2025, 11, 100911.
- [91] J. P. Perdew, K. Burke, M. Ernzerhof, Phys. Rev. Lett. 1996, 77, 3865.
- [92] K. Kim, K. D. Jordan, J. Phys. Chem. 1994, 98, 10089.
- [93] C. J. Cramer, Essentials of Computational Chemistry: Theories and Models, 2nd ed., John Wiley and Sons, Hoboken, NJ 2004.
- [94] J. Heyd, G. E. Scuseria, M. Ernzerhof, J. Chem. Phys. 2003, 118, 8207.
- [95] M. H. Braga, V. Stockhausen, J. C. E. Oliveira, J. A. Ferreira, MRS Online Proc. Library 2013, 1526, 905.